Numerical Simulation of Fluid–Structure Interaction Problem Associated with Vertical Launching System

Younghun Lee*
Seoul National University, Seoul 151-744, Republic of Korea
Min-cheol Gwak†
Agency for Defense Development, Taejon 305-600, Republic of Korea
Heaseong Cho,‡ Hyun Shig Joo,* Sang Joon Shin,§
and Jack J. Yoh¶
Seoul National University, Seoul 151-744, Republic of Korea
and
Jae-Cheol Shin**
Agency for Defense Development, Taejon 305-600, Republic of Korea

DOI: 10.2514/1.A33962

We develop a combined Lagrangian–Eulerian method for transient fluid–structure interaction problems. Based on the ghost fluid framework for improving interface tracking accuracy between a fluid (hot rocket exhaust plume) and a high strain rate deforming solid (rear cover of a vertical launch system), the numerical coupling between the two media ensures an accurate description of the flexible structure. A nine-node quadrilateral element based on total Lagrangian formulation is used, while the hydrodynamic finite difference method is used for the supersonic exhaust plume that forms a complex flow within the plenum. The Lagrangian, Eulerian, and fluid–structure interaction coupling methods are verified by ANSYS results and related theories. A two-dimensional simulation of the full vertical launch system operation mode is conducted. This requires an accurate reproduction of the complex flowfield generated by the rapid rear cover opening under a high-pressure plume during rocket launch. This fluid–structure interaction problem solution may be used for future design upgrades when a vertical launch system is exposed to unusually harsh interactive gas and structure conditions.

Nomenclature

B	=	strain displacement relation matrix
C	=	constituting matrix
d	=	displacement, m
e	=	total energy density, J/kg
F	=	deformation gradient
$\bar{F}$	=	deformation gradient matrix
f	=	force vector, $(\mathrm{kg}\cdot\mathrm{m})/\mathrm{s}^2$
I	=	identity matrix
i	=	x-axis node index
j	=	y-axis node index
k	=	stiffness, kg/s^2
l	=	length, m
$\underline{\underline{M}}$	=	inertial matrix, kg/m^2
m	=	mass, kg
N	=	shape function
$\boldsymbol{n}$	=	normal vector
P	=	pressure, Pa
$\ddot{\boldsymbol{q}}$	=	nodal acceleration vector, m/s^2
R	=	gas constant, $\mathrm{J}/(\mathrm{kg}\cdot\mathrm{K})$
$\boldsymbol{S}$	=	stress vector, Pa
$\bar{S}$	=	second Piola–Kirchhoff stresses, Pa
u	=	velocity, m/s
α	=	relaxation parameter
Γ^e	=	surface domain
γ	=	specific heat ratio
δ	=	plastic multiplier
ε	=	strain
θ	=	degree, rad
ρ	=	density, kg/m^3
σ	=	stress, Pa
Φ	=	yield function equation
ϕ	=	level
Ω^0	=	current domain

Subscripts

e	=	nozzle exit
ext	=	external
g	=	geometric
i	=	internal
k	=	current
x	=	x axis
y	=	y axis
0	=	stagnation

Superscripts

e	=	elastic
$\boldsymbol{n}$	=	current step
p	=	plastic
pl	=	elastoplastic

Received 7 May 2017; revision received 22 January 2018; accepted for publication 9 April 2018; published online 27 June 2018.

*Graduate Research Assistant, Department of Mechanical and Aerospace Engineering.

†Senior Researcher, Department of Mechanical and Aerospace Engineering.

‡Post Doctor, BK21 Plus Transformative Training Program for Creative Mechanical and Aerospace Engineers, Institute of Advanced Machines and Design.

§Professor, Department of Mechanical and Aerospace Engineering, Institute of Advanced Aerospace Technology. Senior Member AIAA.

¶Professor, Department of Mechanical and Aerospace Engineering; jjyoh@snu.ac.kr. Senior Member AIAA (Corresponding Author).

**Principal Researcher.

I. Introduction

IN THE multimaterial analysis of both fluid flow and solid motion, there are different numerical approaches that include Eulerian, Lagrangian, and combined Lagrangian–Eulerian methods. The Eulerian method is used in the calculation of fluid flow [1], while the Lagrangian method is employed to simulate solid dynamics [2]. To use the advantages of both methods, a combined Lagrangian–Eulerian method [3–10] has been in use for the integrated analysis of complex interactions between fluids and solids.

Using the combined method as an interface treatment methodology, the remeshing technique [10] of arbitrary Lagrangian–Eulerian and the particle level-set method using the ghost fluid concept [3,5,11] are proposed. The remeshing composes a new mesh in the Eulerian domain, based on a Lagrangian domain boundary surface when a solid structure is changed. Since the method fundamentally operates in an unstructured grid, the numerical accuracy is secured by increasing the number of grid cells in a high-gradient domain. However, in the case of a large deformation problem, the method is barely suitable for calculation due to the accumulated numerical errors and high computational costs associated with determining the values in the newly generated grids. On the other hand, the particle level-set method with a ghost node concept can efficiently discriminate the interface between Eulerian and Lagrangian domains in transient fluid–structure interaction (FSI) problems. This is quite evident in various studies that use the combined Lagrangian–Eulerian methods [3–6].

In this paper, we consider a large deformation problem using a combined Lagrangian–Eulerian method based on the immersed boundary method for a multimaterial problem [12–14] and the hybrid particle level-set method for tracking material interface motion [15]. The ghost nodes are defined in the neighboring material of a real material based on the isentropic theory. A level-set zero denotes the Lagrangian domain boundary for Eulerian calculation, and the total pressure transformation in the Eulerian domain to a loading force in Lagrangian domain is performed with a separate algorithm.

This method is applied to a large deformation problem occurring when a vertical launch system (VLS) rear cover opens and closes. During VLS operation, the rear cover rapidly deforms in milliseconds when opening at the high temperature (~2000 K) and pressure (6 bar) of the launch vehicle exhaust. Previously, for safety reasons, the fixed rear cover was analyzed in closed and opened states, and the plume dynamics were calculated in one-, two- [16–18] and three-dimensional simulations [19,20]. In this case, the rear cover deformation was not considered in the flow dynamics coupled with rocket structural changes during launch. Therefore, the rear cover pressure load induced from the exhaust plume was not calculated. In this work, the strongly coupled FSI between the rocket plume and the rear cover undergoing large deformation during opening and closing makes it possible to predict the resulting pressure distribution within the plenum. This also allows estimating the closing time for the neighboring rear cover in a paired VLS fresh launch.

II. Numerical Model

A. Governing Equations for Fluid

The compressible gas dynamic equations for simulating the ammonium perchlorate (AP) based rocket plume in a two-dimensional rectangular coordinate system consist of the mass, momentum, and energy balance laws as

$$\frac{\partial U}{\partial t} + \frac{\partial G}{\partial x} + \frac{\partial F}{\partial y} = 0 \tag{1}$$

$$\begin{aligned} U &= (\rho, \rho u_x, \rho u_y, \rho e)^T \\ G &= (\rho u_x, \rho u_x^2 + P, \rho u_x u_y, u_x(\rho e + P))^T \\ F &= (\rho u_y, \rho u_x u_y, \rho u_y^2 + P, u_y(\rho e + P))^T \end{aligned} \tag{2}$$

where ρ, u_x, u_y, and P are the density, x-axis velocity, y-axis velocity, and pressure, respectively. The governing equations are solved by a third-order Runge–Kutta and convex essentially nonoscillatory method in the temporal and spatial discretizations, respectively [14].

B. Governing Equations for Structure

The rear VLS cover is a thin metallic plate forced open by the high-pressure plume during rocket launch. The rear cover also runs into a rigid wall when it is fully open. Hence, the rear cover undergoes geometric and material nonlinear behavior. The relevant contact algorithm for handling this nonlinearity consists of a nine-node quadrilateral element for the flexible structure and a rigid-body dynamic analysis for the inflexible structure.

1. Flexible Structure Model

A nine-node quadrilateral element based on the total Lagrangian formulation is used to capture the geometrically nonlinear behavior [21] and is further extended to predict the materially nonlinear behavior. All element quantities in the total Lagrangian description are expressed with respect to the initial configuration. Using the deformation gradient, Green–Lagrange strain components are defined, and the relevant stresses are then calculated by the constituting equation. The following relationship is applied for elastic analysis. For plastic analysis, the defining strain components and the constituting matrix need to be modified,

$$\begin{aligned} \boldsymbol{S} &= C\{\varepsilon_{xx} \quad \varepsilon_{yy} \quad 2\varepsilon_{xy}\}^T = \{\sigma_{xx} \quad \sigma_{yy} \quad \sigma_{xy}\}^T, \\ (1/2)(F^T F - I) &= \{\varepsilon_{xx} \quad \varepsilon_{yy} \quad \varepsilon_{xy}\}^T \end{aligned} \tag{3}$$

$$\bar{S} = \begin{bmatrix} \hat{S} & 0 \\ 0 & \hat{S} \end{bmatrix}, \qquad \hat{S} = \begin{bmatrix} \sigma_{xx} & \sigma_{xy} \\ \sigma_{xy} & \sigma_{yy} \end{bmatrix} \tag{4}$$

where $\boldsymbol{S}$, C, ε, σ, F, I, and $\bar{S}$ are stress vector, constituting matrix, strain, stress, deformation gradient, identity matrix, and second Piola–Kirchhoff (PK) stresses, respectively.

Virtual work linearization can be expressed by taking the deformation gradients and the second PK stresses into account,

$$(k_g + k_h)\Delta d = -\boldsymbol{f}_i + \boldsymbol{f}_{\text{ext}} \tag{5a}$$

$$\begin{aligned} &\left(\iint_{\Omega^0} B\bar{S}B^T \,\mathrm{d}\Omega^0 + \iint_{\Omega^0} B\bar{F}^T C\bar{F}B^T \,\mathrm{d}\Omega^0\right)\Delta d \\ &\quad = -\iint_{\Omega^0} B\bar{F}^T \boldsymbol{S} \,\mathrm{d}\Omega^0 + \boldsymbol{f}_{\text{ext}} \end{aligned} \tag{5b}$$

where k_g, k_h, d, $\boldsymbol{f}_i$, $\boldsymbol{f}_{\text{ext}}$, B, $\boldsymbol{S}$, C, $\bar{F}$, and Ω are the geometric stiffness matrix, current stiffness matrix, displacement, internal force vector, external force vector, strain displacement relation matrix, second PK stresses matrix, constitutive matrix, deformation gradient matrix, and current domain, respectively. The external load vector defined by pressure loading from fluid analysis is

$$\boldsymbol{f}_{\text{ext}} = \int_{\Gamma^e} N^T p \,\mathrm{d}\Gamma^e, \qquad p = \{p_x \quad p_y \quad 0\}^T \tag{6}$$

where N, p, and Γ are elemental shape function, pressure, and surface domain, respectively.

The plane stress projected plasticity model based on the incremental plastic flow prediction and a von Mises equation with isotropic hardening is used to calculate the rear cover material nonlinearity [22]. This approach is appropriate for elastoplasticity in a metallic structure

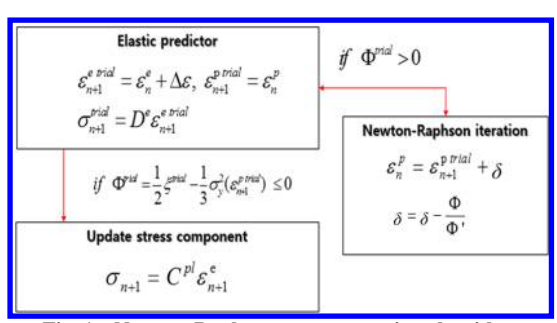

Fig. 1 Newton–Raphson return mapping algorithm.

that undergoes large displacement and small strain. This plastic model, the updated strain, and stress components are used in Eq. (5b).

In Fig. 1, the defined elastic strain ε, the corresponding trial strain $\varepsilon^{e\,\mathrm{trial}}$, and the accumulated plastic strain $\varepsilon^{p\,\mathrm{trial}}$ are calculated to check for plastic admissibility. To comply with the von Mises model, a yield function equation Φ is used. The detailed mathematics and the relevant descriptions are described in Ref. [22]. For time transient analysis, the Hilbert–Hughes–Taylor α method is used. The final form of the governing equation for the flexible structure is

$$(1+\alpha)(\boldsymbol{f}_{\mathrm{ext}}^{n+1} - \boldsymbol{f}_i^{n+1}) - \underline{\underline{M}}\ddot{\boldsymbol{q}}_g^{n+1} + \alpha(\boldsymbol{f}_i^{n} - \boldsymbol{f}_{\mathrm{ext}}^{n}) = 0 \tag{7}$$

Here, the inertial matrix $\underline{\underline{M}}$ is defined using the elemental shape function, $\underline{\underline{M}} = \rho\int_\Omega \underline{\underline{N}}^T N\,\mathrm{d}\Omega$, and f_i is the internal load vector defined by the right side of Eq. (5a). The contact analysis is based on the global Lagrange multiplier. This approach is realized by multiplying the gap condition. The gap condition is defined by the position of slave and master bodies.

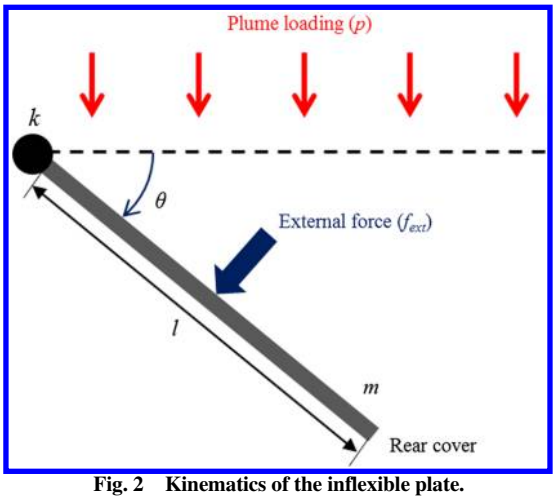

Fig. 2 Kinematics of the inflexible plate.

2. *Inflexible Structure Model*

To predict inflexible structure behavior, a rigid plate motion equation is developed. The plate is assumed to have only in-plane rotational degrees of freedom under a rotational spring boundary condition.

Figure 2 shows the relevant boundary condition and kinematics of the rear cover inflexible plate. The plate governing equation is defined by a second-order differential equation in terms of the rotational degrees of freedom. It is expressed by taking the mass m and length l of the plate and rigidity of spring boundary k into account:

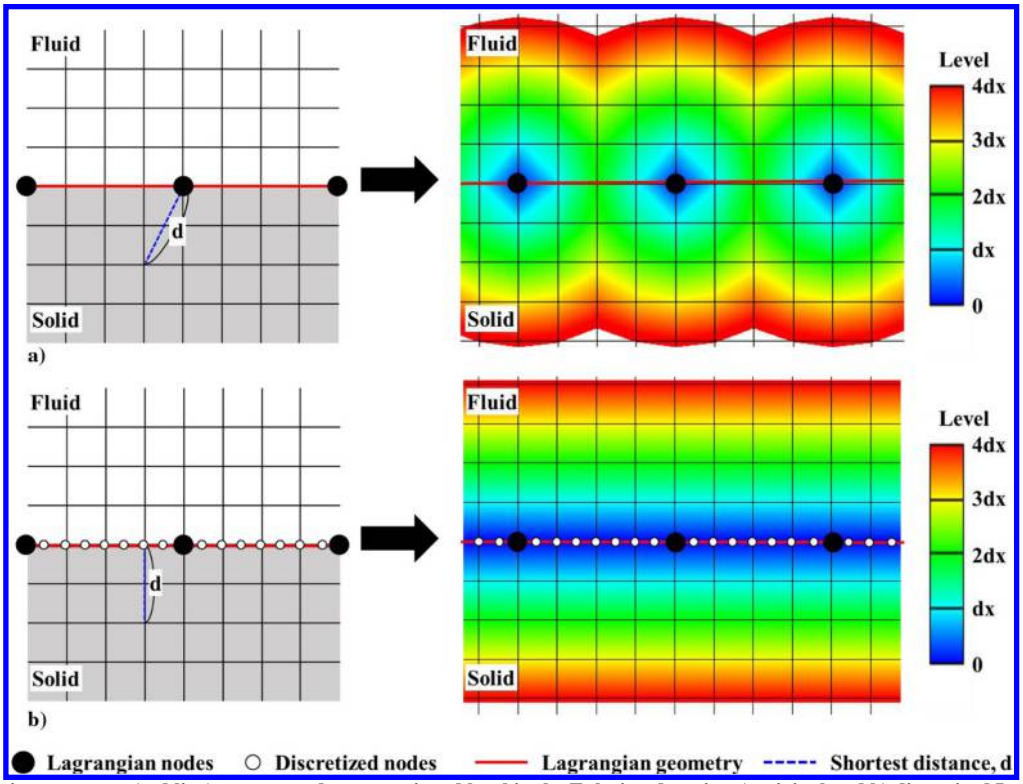

Fig. 3 Lagrangian geometry (red line) represented as an unsigned level in the Eulerian domain: a) original and b) discretized Lagrangian nodes.

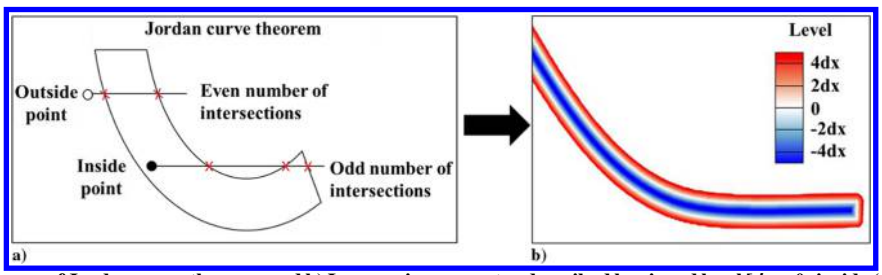

Fig. 4 a) Conceptual diagram of Jordan curve theorem and b) Lagrangian geometry described by signed level [$\phi < 0$: inside (solid, blue); $\phi > 0$: outside (fluid, red); $\phi = 0$: interface (white line)] in Eulerian domain.

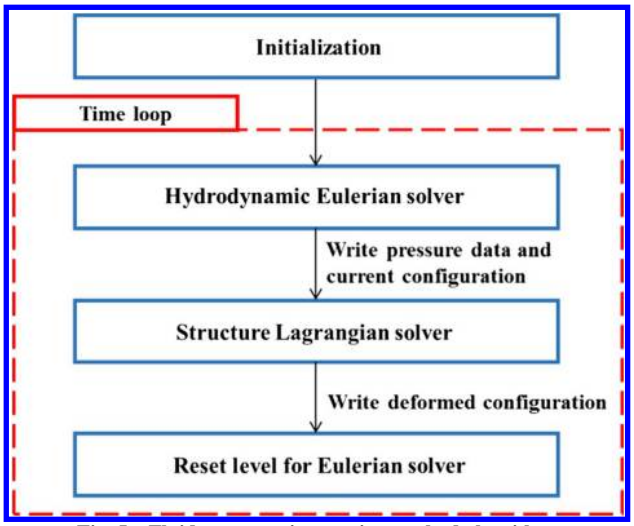

Fig. 5 Fluid structure interaction method algorithm.

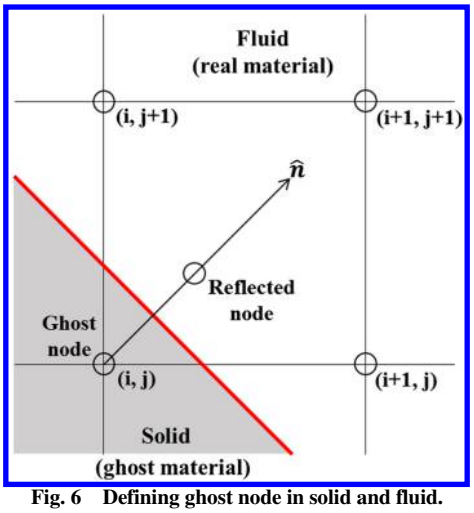

Fig. 6 Defining ghost node in solid and fluid.

$$\frac{ml}{2}\ddot{\theta} + k\theta - f_{\text{ext}} = 0 \tag{8}$$

A modified contact algorithm is developed for the inflexible structure. This modified algorithm does not fully exploit the contact mechanics, i.e., impact and rebound. However, the plate is under a fixed boundary condition when it is near the rigid wall.

C. Strongly Coupled Fluid–Structure Interaction Approach

To track the interface and define the boundary value between the hot rocket plume and the rear cover, a level-set method based on the ghost fluid method (GFM) is applied [15]. The level ϕ defines a distance of each material surface from the contact interface. So, the zero level ($\phi = 0$) represents the interface of the two materials, and the signs of level classify the material, meaning the region with $\phi < 0$ indicates the inner side of the target material that is either a fluid or solid. At the interface, the boundary conditions are determined by the GFM. The properties of ghost nodes are addressed by the values of symmetric real nodes, which are determined by extrapolation. At the ghost nodes, the normal to the interface is calculated by

$$\boldsymbol{n} = \frac{\nabla\phi}{|\nabla\phi|} \tag{9}$$

Table 1 Material properties of cantilever beam (304 stainless steel)

Parameter	304 stainless steel
Initial density, kg/m^3	7800
Poison's ratio	0.29
Young's modulus, GPa	205
Initial yield strength, MPa	215
Hardening coefficient, GPa	50

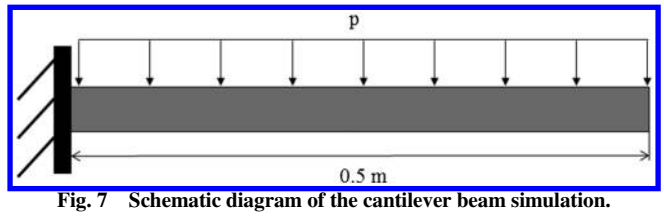

Fig. 7 Schematic diagram of the cantilever beam simulation.

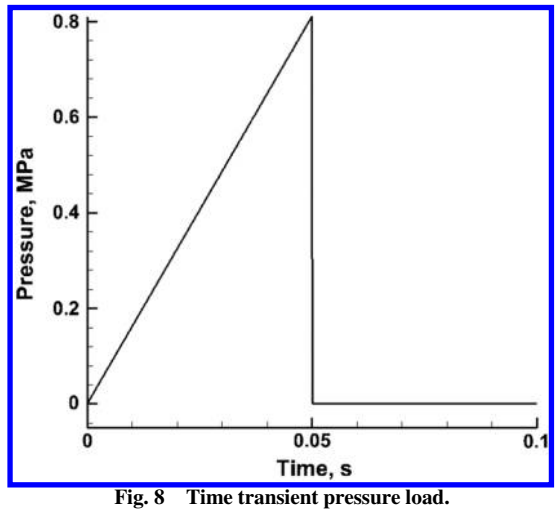

Fig. 8 Time transient pressure load.

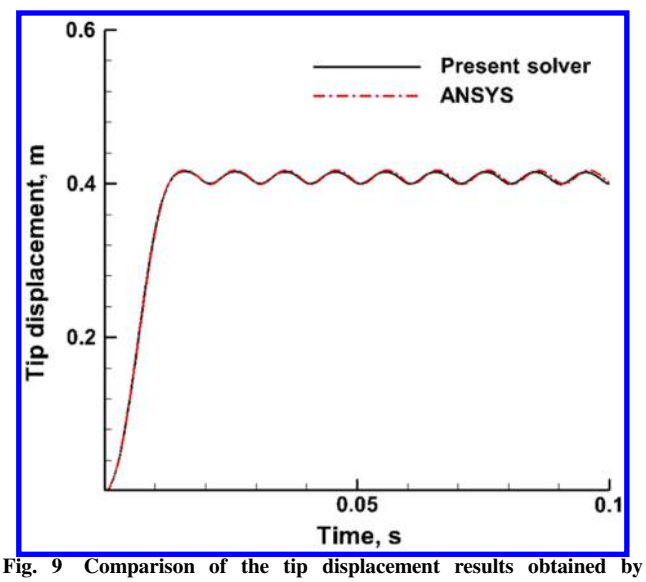

Fig. 9 Comparison of the tip displacement results obtained by Lagrangian method and ANSYS.

Table 2 Setup of shock tube problem

Initial condition	Density, kg/m^3	Velocity, m/s	Pressure, bar	Gamma
Left side ($x < 0.6$)	0.384	27.077	100	1.667
Right side ($x > 0.6$)	100	0	1	3.0

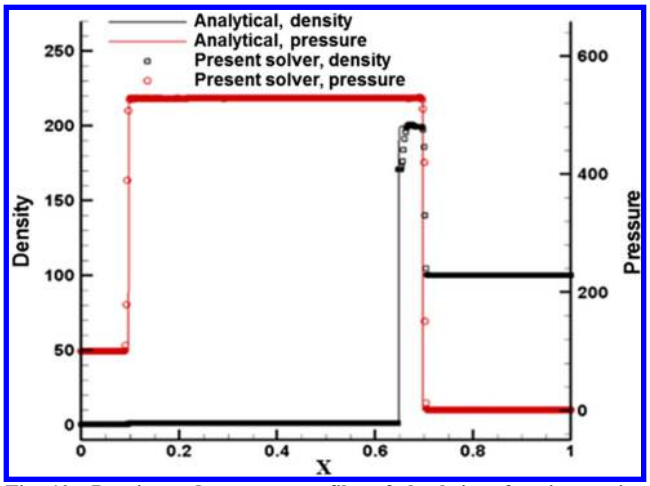

Fig. 10 Density and pressure profiles of shock interface interaction problem at 0.03 s.

In the previous studies, the level is updated by the particle velocity of materials, and the mesh size of both materials is similar [1–5]. In this paper, however, the Lagrangian geometry is replaced with the Eulerian level sets in order to apply the GFM. Although fine grids are necessary for handling the complex supersonic flow inside the VLS, the rear cover motion can be simulated with a relatively coarse mesh. If the distance between the Lagrangian nodes is larger than the Eulerian mesh size, the level is represented as Fig. 3a. The interface ($\phi = 0$, blue) does not appear as a line, and a normal vector to the boundary at each Eulerian node is not defined. So, one discretizes the Lagrangian nodes as white dots. The white dots are artificial Lagrangian nodes that define the intended Lagrangian geometry in terms of Eulerian quantity. The distance between the white dots is one-half of the Eulerian mesh size, and the level is converted as in Fig. 3b. The interface and normal vectors are clearly defined, and thus the ghost node values can be determined.

To set different signs for each material, the Jordan curve theorem [23] is applied. In Fig. 4a, the sign of the interior level is negative when the number of point is odd, where the straight line starting from an inner point intersects the boundary. In the opposite case, the level sign is positive. Using this approach in the Eulerian domain, the Lagrangian geometry described by the signed level is shown as in Fig. 4b.

To unify a hydrodynamic Eulerian solver for a plume and a Lagrangian solver for a nonlinear rear cover, the outline of the developed algorithm is as in Fig. 5.

Initially, the fluid flow and solid dynamics are described in the Eulerian configuration. The outer boundary of the structure is represented by the level sets, and the boundary conditions are determined by the values of the ghost nodes. Then, the fluid flow is solved by the Eulerian solver. The ghost node values are obtained by the real material, while normal and tangential velocities are calculated. Figure 6 shows the schematic of two-dimensional GFM for a fluid and solid [15,17]. The calculated total pressure near the Lagrangian nodes is used as the boundary value update for the external force in Eq. (6) for a Lagrangian solver. The solver calculates the deformed geometry and converts it into a level in the next time step. The Eulerian and Lagrangian steps are strongly coupled in this sense, and the pressure and geometry data are exchanged at every time step to minimize the numerical errors in the unified simulation.

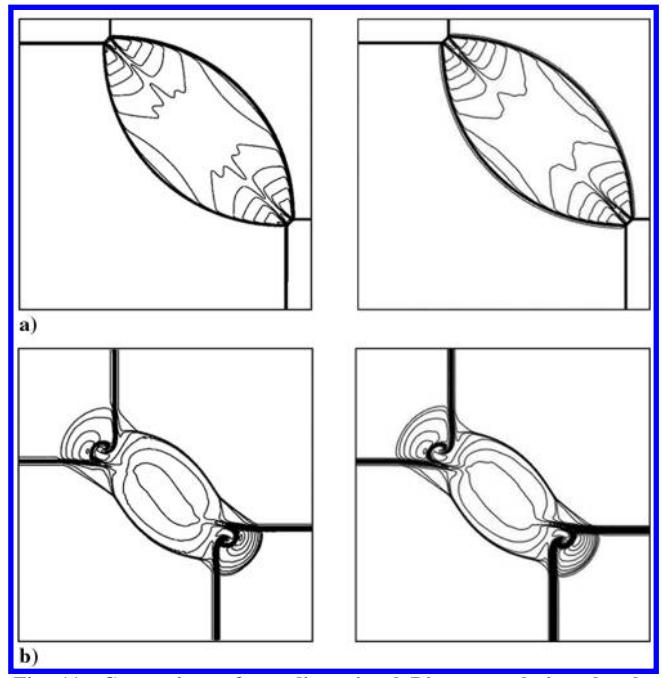

Fig. 11 Comparison of two-dimensional Riemann solutions by the present solver (right) and the Ref. [24] (left) showing density contour for a) case 1 and b) case 2.

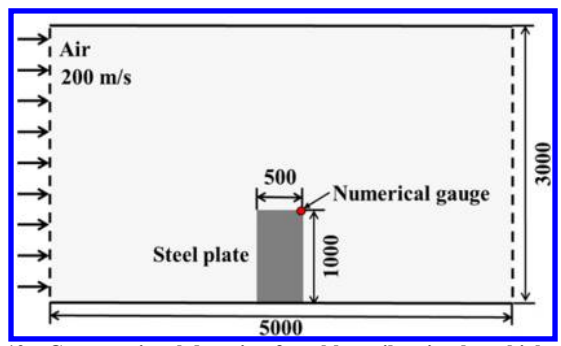

Fig. 12 Computational domain of steel bar vibration by a high-speed uniform flow (length unit: mm).

III. Validation

A. Lagrangian Method

The Lagrangian solver for the flexible structure is validated against the ANSYS prediction. A cantilever beam in the two-dimensional domain is considered, and the beam is subjected by a time transient pressure loading. The properties of the cantilever beam are summarized in Table 1. The geometry and loading conditions are depicted in Fig. 7 with Fig. 8 showing the relevant time transient pressure loading conditions. The beam structure is discretized by 16 quadrilateral elements. Tip displacement history is compared with the ANSYS prediction. Figure 9 shows the relevant comparison between our result and the ANSYS result. The comparison results are in good agreement.

Table 3 Setup of two-dimensional Riemann problems

		Left side initial condition ($x < 0.5$)				Right side initial condition ($x > 0.5$)			
Case		Pressure, bar	Density, kg/m^3	u_x, m/s	u_y, m/s	Pressure, bar	Density, kg/m^3	u_x, m/s	u_y, m/s
1	Upper side ($y > 0.5$)	0.35	0.5065	0.8939	0	1.1	1.1	0	0
	Lower side ($y < 0.5$)	1.1	1.1	0.8939	0.8939	0.35	0.5065	0	0.8939
2	Upper side ($y > 0.5$)	1	2	−0.75	0.5	1	1	−0.75	−0.5
	Lower side ($y < 0.5$)	1	1	0.75	0.5	1	3	0.75	−0.5

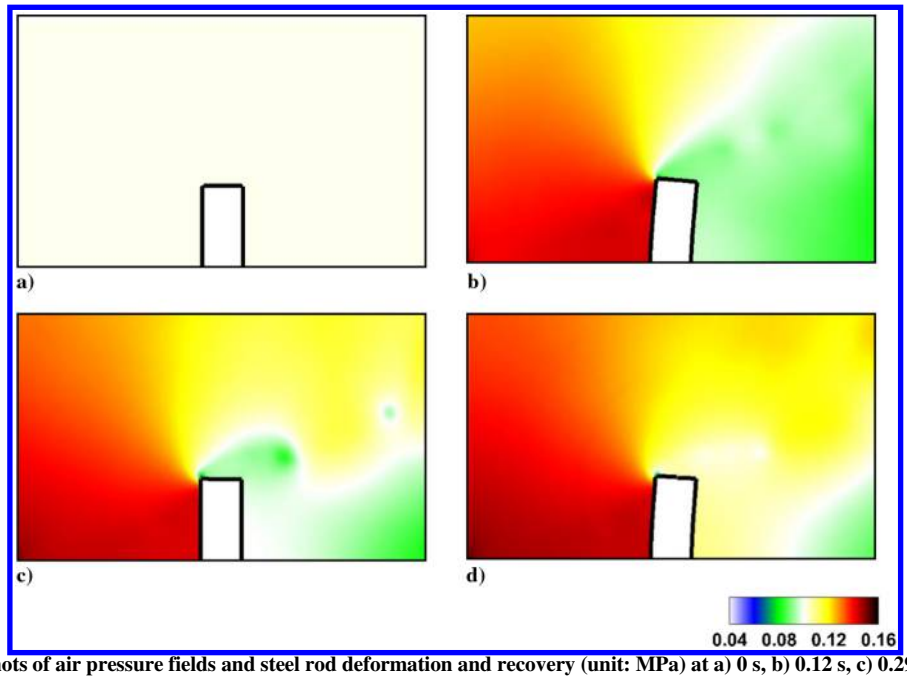

Fig. 13 Snapshots of air pressure fields and steel rod deformation and recovery (unit: MPa) at a) 0 s, b) 0.12 s, c) 0.29 s, and d) 0.44 s.

B. Eulerian Method with Ghost Fluid Treatment

For accuracy of plume dynamic and related FSI treatment, we set up a shock tube problem consisting of two different gases of distinct initial conditions [13] as shown in Table 2. Heavy gas is on the right side ($x > 0.6$), while the lower-density gas is initially impacted by a planar velocity of 27.077 m/s on the left. The necessary grid resolution is less than 2 mm, and we have chosen 1 mm in the simulation. The initial membrane breakage occurs at position 0.6, and Fig. 10 shows the pressure and density profiles that result at 0.3 s. In this figure, reflected and transmitted shock wave speeds are shown. The calculated state variables are compared against the analytical solution.

To validate the plume dynamics in two dimensions, we additionally consider multidimensional Riemann problems [24]. The problems consist of four different initial conditions in each quadrant as specified in Table 3. Conventional ideal gas assumption is used with a specific heat ratio $\gamma = 1.4$. Two cases are considered, and the results are validated against the reference as shown in Fig. 11, showing an excellent agreement.

To validate the strongly coupled FSI, we consider elastic vibration of a steel rod subjected to a high-velocity fluid flow. The initial condition and two-dimensional computational domains are shown in Fig. 12. The boundary conditions on the top, bottom, left, and right are all outflows (or zero-gradient boundaries), slip, inflow (200 m/s), and outflow conditions, respectively. The 304 stainless steel parameters are as listed in Table 1.

Figure 13 shows the fluid pressure field and the elastic deformation recovery of the steel rod for increasing time sequences. In Fig. 13b, the steel rod is bent by the uniform flow from the left, and the pressure increase is shown in the front tip of the rod. Figure 13c is the elastic recovery that resets the bent rod back to the initial position. In the rear and top regions of the rod, the fluid pressure field is consistently changed in accordance with rod vibration. A gauge is placed at the edge of the rod, and the results are compared with the ANSYS

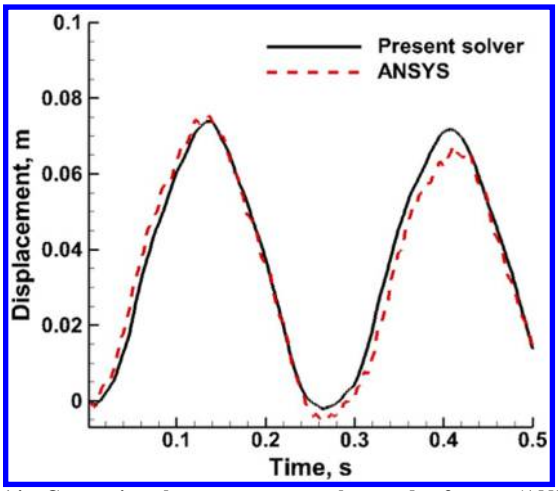

Fig. 14 Comparison between present solver and reference (ANSYS) using displacement histories in each numerical gauge.

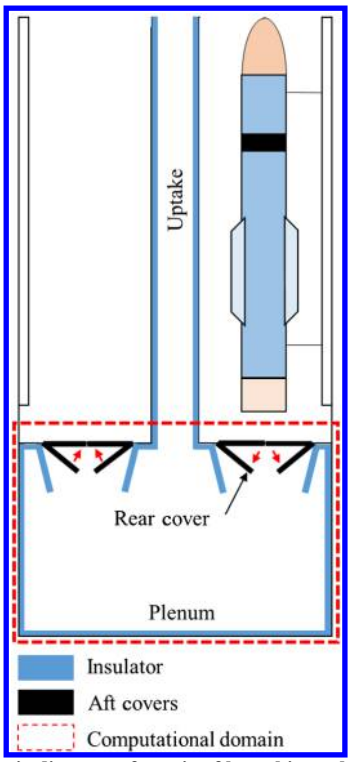

Fig. 15 Schematic diagram of a pair of launching tubes, separated by the plume exhaust uptake.

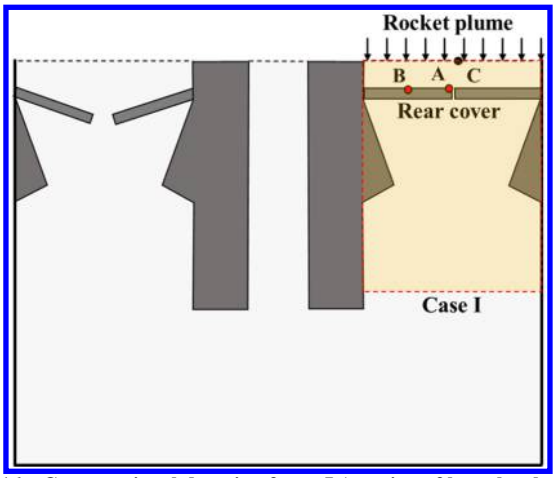

Fig. 16 Computational domain of case I (opening of launch tube rear cover) and case II (closure of opened rear cover of left launch tube).

prediction. Figure 14 shows that the rod displacement compared to ANSYS is quite similar with the maximum displacement of 0.078 mm and frequency of 3.7 Hz.

IV. Results and Discussion

Using the combined Lagrangian–Eulerian method based on strongly coupled FSI, we simulated the dynamic motion of the rear-end cover of a launch canister as installed on a surface battleship that stores missile canisters below deck in a ready-to-fire condition. Figure 15 shows the canister cross-section view. When the missile is fired, the rear cover is deformed by the high-pressure exhaust plume that fills the lower plenum with strong acoustic and shock waves that are reflected and transmitted.

In this paper, the rear cover deformation due to the exhaust plume is a major concern. However, a three-dimensional VLS simulation with strong FSI demands an extremely high cost for simulation. Alternatively, the problem is reconfigured in two dimensions as shown in Fig. 15. Here, we cut VLS along the center axis of the two canisters to consider the opening and closing of the rear covers. In each, the dynamics of plumes inside and the deformation of each rear cover (either open or closed) can also be represented by the

Table 4 Rocket plume composition AP/HTPB propellant for NASA chemical equilibrium applications code input

Parameter	AP/HTPB [25]
Mole fraction of CO	0.26995
Mole fraction of CO_2	0.04621
Mole fraction of Cl	0.00048
Mole fraction of H	0.00105
Mole fraction of HCl	0.14745
Mole fraction of H_2	0.22737
Mole fraction of H_2O	0.23329
Mole fraction of NH_3	0.00002
Mole fraction of N_2	0.07395
Mole fraction of OH	0.00021

Table 5 Rocket plume parameters obtained from NASA chemical equilibrium applications code calculation

Parameters	NASA CEA [26]
Specific heat ratio γ	1.245
Gas constant R, $\mathrm{J/(kg \cdot K)}$	382.7
Stagnation pressure p_0, bar	76.86
Stagnation temperature T_0, K	2155

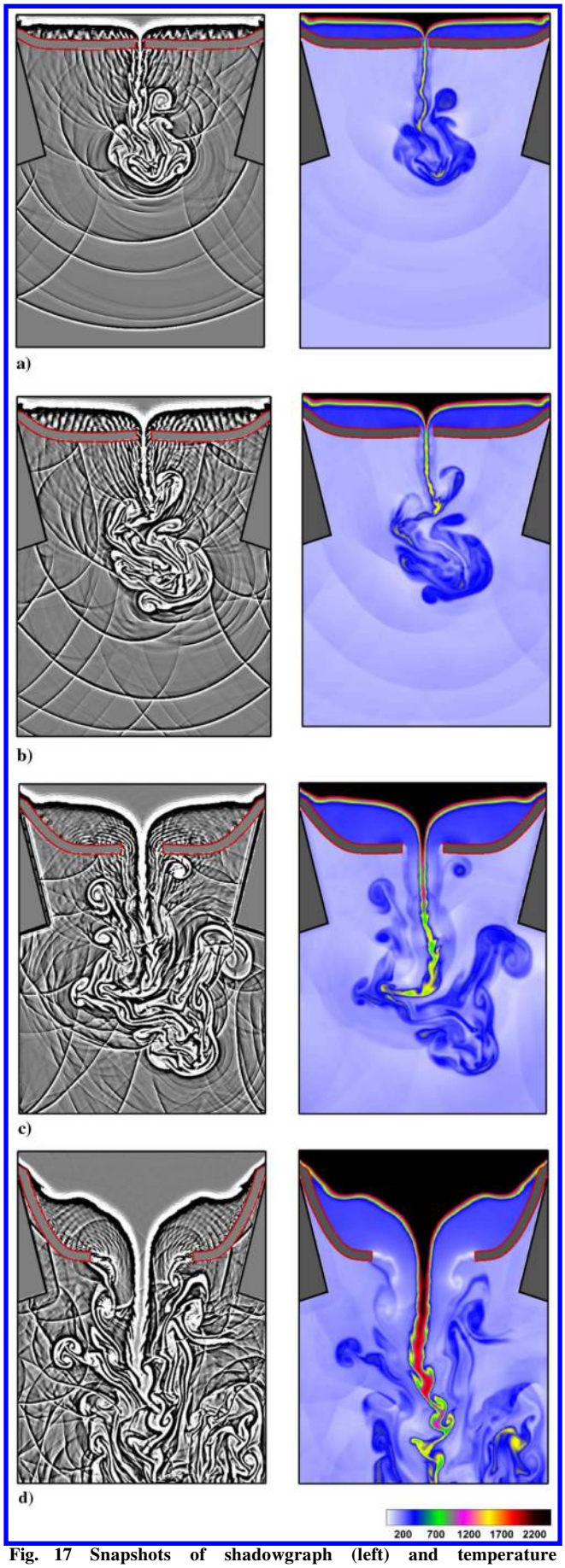

Fig. 17 Snapshots of shadowgraph (left) and temperature (unit: K) fields (right) coupled to the elastoplastic rear cover during opening at a) 1.5 m · s, b) 2.0 m · s, c) 3.0 m · s, and d) 4.0 m · s.

two-dimensional flow. Case I is the opening of the rear cover during the rocket launch. Case II is the closing of the rear cover by the plenum pressure. In case I, the rear cover is considered as either an elastoplastic plate or an inflexible plate that is fixed to a spring hinge. Both are simulated under the same loading by the rocket exhaust plume, and different plume flows are observed.

Since there are no measured data of pressure or temperature in the plenum for monitoring the rear cover dynamics, the numerical simulation based on the modeled AP propellant combustion and subsequent pressure loading of the plume is used to understand the cover behavior. In case II, we only consider the inflexible plate because the real rear cover is composed of both steel and a composite insulator. As the insulator is brittle and thicker than the steel cover, the deformation behavior of the rear cover is considered inflexible.

A. Incoming Rocket Plume Initialization and Transient Boundary Update

Figure 16 shows the calculation domain of the VLS, and in particular the boundary conditions around the red-dotted region for case I are defined. In the figure, the solid line defines the wall boundary, while the dashed line is the zero-gradient flow out condition. The top boundary is the incoming flow condition in which the rocket exhaust plume is dispersed. A reacted or product gas of the AP/HTPB composite propellants rocket plume is considered to be composed of the elements listed in Table 4. Using the plume gas composition, the initial density, velocity, temperature, and pressure of the hot product gas from the exhaust nozzle can be defined.

The incoming velocity of the plume is determined by Eq. (10) by assuming the isentropic flow in a converging–diverging nozzle and the steady-state condition of the combustion chamber, neither of which is included in the calculation domain,

$$u_e(t) = \sqrt{2\left(\frac{\gamma R}{\gamma - 1}\right) T_0 \left[1 - \left(\frac{p_e(t)}{p_0}\right)^{(\gamma-1)/\gamma}\right]} \tag{10}$$

Here, u_e, t, γ, R, T_0, p_e, and p_0 are the nozzle exit velocity or the plume velocity, time, specific heat ratio, gas constant, stagnation temperature, plume pressure, and stagnation pressure, respectively. Table 5 summarizes the rocket plume parameters obtained by running the NASA CEA code using the presumed mole fractions in Table 4 [25,26].

The initial plume pressure $p_e(0)$ at position C in Fig. 16 is assigned 1 bar at 2000 K and Mach number 2.3, with the initial density defined by the ideal gas equation of state. At every time step update, the transient incoming plume boundary condition is determined by Eq. (10) with $u_e(t)$ extrapolated from position C in Fig. 16.

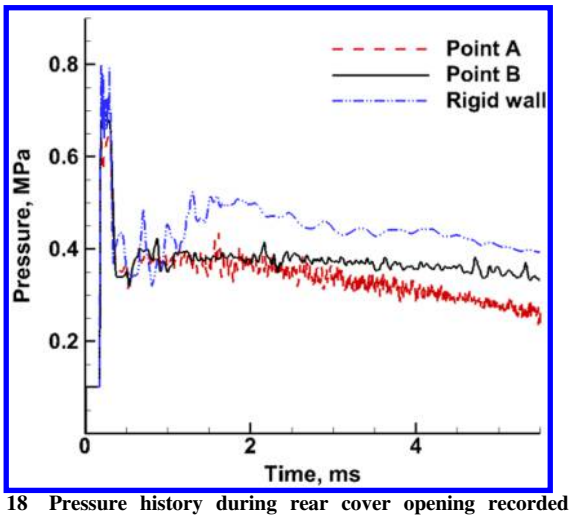

Fig. 18 Pressure history during rear cover opening recorded at positions A and B. Rigid wall corresponds to a pressure if both covers are assumed rigid and remained closed at all times.

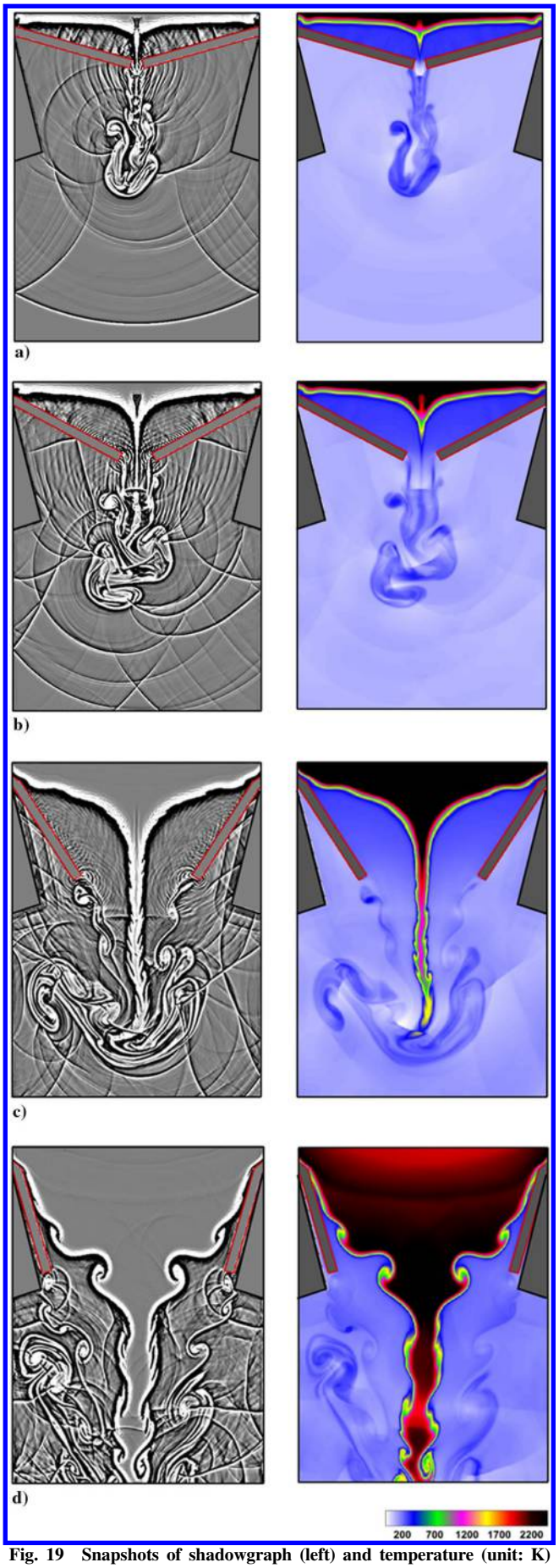

Fig. 19 Snapshots of shadowgraph (left) and temperature (unit: K) fields (right) coupled to the inflexible rear cover during opening at a) 1.5 m · s, b) 2.0 m · s, c) 3.0 m · s, and d) 4.0 m · s.

B. Case I: Opening of Rear Cover During Rocket Launch

The numerical simulation of the rocket plume loaded onto the elastoplastic rear cover was performed. Figure 17 shows the shadowgraph and temperature contours at 1.5, 2, 3, and 4 m · s. In these figures, the complex plume dynamics and reflected acoustic waves are shown during the rear cover opening. Two interesting points evident in the simulation are the contact surface formation and the jet flow through the opening rear covers. The contact surface between the high-temperature rocket plume and the cold air above the cover was observed and remained at all times. Noticeably, the hot plume gas never touched the cover plate during opening. Therefore, any temperature effect on the metal deformation may have been neglected. This finding that thermal deformation does not play a significant role is important. The resulting jet forms a nozzle that allows hot gases to bypass the metal covers during the launch. From Fig. 17, one can see that then rear cover deformation pattern gave rise to the jet flow pattern, resulting in a very complex flow and acoustic fields in the plenum.

The real source of rear cover deformation was the compressive force of the rocket plume. So, we take into account the pressure on rigid (closed) rear covers and compare that to the elastoplastic rear covers. Figure 18 shows the history of pressure readings at the rigid wall and two deformation plate locations. The fluid velocity near the wall became zero during the impact, and the pressure was doubled. After 0.2 m · s, the pressure reached 4 atm, which is twice the plume pressure, and remained at a high value. In the elastoplastic plate cases, the pressure started to decrease once the plate opened and deformed. In particular, the pressure near the side wall (point B) was higher than the pressure at the plate tip (point A) because the flow velocity in the proximity of the tip was higher than at the nearby side wall. This indicates that the pressure boundary conditions for the Lagrangian solver were not uniform, and experimentally obtained pressure data would be invaluable for enhanced future calculations.

Next, we consider the inflexible rear cover plate deformation by a fully reacted rocket plume. Figure 19 shows the shadowgraph and temperature contours at 1.5, 2, 3, and 4 m · s. In this figure, the angular speed of the rear cover is almost the same as that of the elastoplastic case, but the tip deformation speed is approximately three times faster. Therefore, the jet flow due to the hot rocket plume is not seen in the inflexible plate case as shown in Fig. 19b. It is seen in the flexible plate case shown in Fig. 17b, although though the contact surface and shock propagation of both plates are nearly identical in the early stages. However, later in the inflexible plate case, which opens more quickly, the velocity of the rocket plume increases. This can be seen by comparing Figs. 17d and 19d. These observations point to the differences in plume speed and temperature distribution near the tip in each simulation. The rocket plume can ablate the VLS structure. Therefore, predicting the rocket plume around the structure is quite essential, especially around the rear cover and bottom of the VLS.

Because of the severity of the detection environment near the rear cover, actual experimental data do not exist, except for the total deforming time, which was reported to be about 4 m · s. In the simulations, the deforming time was calculated as 4.3 m · s in the

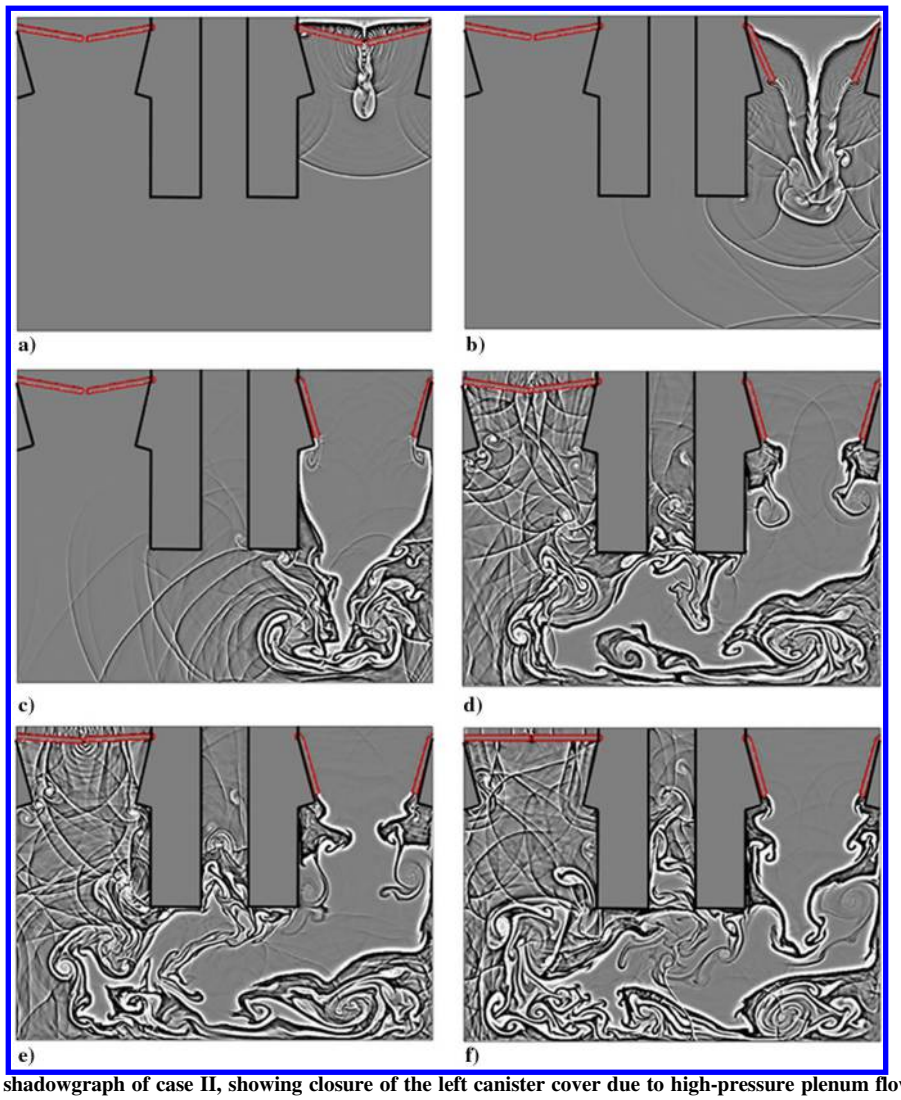

Fig. 20 Full simulation shadowgraph of case II, showing closure of the left canister cover due to high-pressure plenum flow at a) 1 m · s, b) 3 m · s, c) 4.8 m · s, d) 7 m · s, e) 7.4 m · s, and f) 8 m · s.

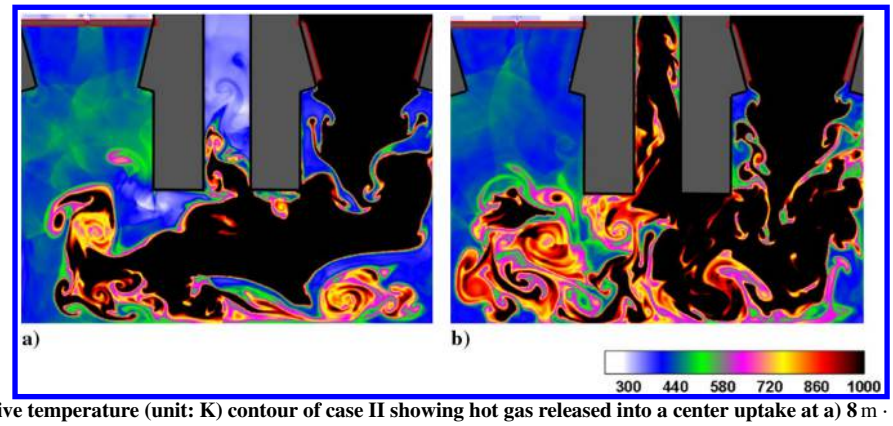

Fig. 21 Selective temperature (unit: K) contour of case II showing hot gas released into a center uptake at a) 8 m · s and b) 10 m · s.

flexible case and 3.8 m · s in the inflexible case. Therefore, the solid properties and pressure loading by the hot rocket plume were reasonable, and simulation results can predict the flow conditions inside of VLS.

C. Case II: Closure of Opened Rear Cover After Launch

To estimate the time elapsed for closure of the opened rear covers (on the left tube) by the launch of a fresh VLS tube (on the right), an extended domain is considered in Fig. 16. Only the inflexible rear cover is considered in the full calculation. The plume boundary condition on the top, initial conditions, and material properties are identical to case I.

Figure 20 shows the hot gas propagation led by multiple shock waves through the shadowgraphs. In the early stages (Figs. 20a and 20b), complex plume flow and reflected and transmitted shock waves were generated during the opening of the right-side launch tube. In Figs. 20c and 20d, a series of shock waves propagate toward the right-side launch tube, followed by the distorted plume flows that also arrive at the used rear covers on the left. The primary shock wave, which exerts an external force on the rear covers, pushes the cover to its original position and shuts it closed. This closure occurred at about 7–8 m · s when the hot covers were completely closed as shown Figs. 20d–20f. Once closed, the hot gas plume had to find an alternative exit to depressurize and leave through the center uptake as shown in Fig. 21 in the temperature contour. The hot gas or the flame speed through this uptake can be estimated from Fig. 21b, knowing the time elapsed and the length of the uptake chamber. The thermal condition in the plenum as well as maximum temperature induced near the rear cover were well predicted to be ∼2000 K at 4–5 m · s. This simulated thermal distribution is also useful for the design of any VLS insulator. Without the strongly coupled strategy for a combined Lagrangian–Eulerian method, various hydrodynamic phenomena induced by transient structural changes, including the opening and closing of VLS rear covers by a hot rocket plume, would not have been captured and understood.

V. Conclusions

This paper has developed an algorithm for coupling the Lagrangian and Eulerian methods to simulate the severely transient fluid–structure interaction problem that arises during the operation of vertical launch tubes. The opening of tube rear covers due to ammonium perchlorate propellant burning gases was dynamically reproduced. The resulting plume that fills the lower plenum was analyzed to understand the hydrodynamic state of the gas-filled plenum subjected to the structural motions of the deforming rear covers. The coupled algorithm and its ability to handle strongly coupled multimaterial interactions were verified by the theories and ANSYS solutions. The validated method was used to reproduce the hydrodynamic and thermal flowfields inside the plenum during launch tube operation. Future vertical launch system designs that are exposed to unusually harsh interacting fluid and structure conditions can benefit from the results outlined in this paper.

Acknowledgments

This work was conducted at High-Speed Vehicle Research Center with the support of Defense Acquisition Program Administration and Agency for Defense Development under contract number UD170018CD contracted through IAAT at Seoul National University.

References

[1] Wellington, C., Alexandra, M. R., Marcio, R. P., Millena, M. V., and Aristeu, S., "A 3D Front-Tracking Approach for Simulation of a Two-Phase Fluid with Insoluble Surfactant," *Journal of Computational Physics*, Vol. 281, Jan. 2015, pp. 403–420. doi:10.1016/j.jcp.2014.10.021

[2] Sambasivan, S. K., Shashkov, M. J., and Burton, D. E., "A Cell-Centered Lagrangian Finite Volume Approach for Computing Elasto-Plastic Response of Solids in Cylindrical Axisymmetric Geometries," *Journal of Computational Physics*, Vol. 237, March 2013, pp. 251–288. doi:10.1016/j.jcp.2012.11.044

[3] Souli, M., Ouahsine, A., and Lewin, L., "ALE Formulation for Fluid-Structure Interaction Problems," *Computer Methods in Applied Mechanics and Engineering*, Vol. 190, Nos. 5–7, 2000, pp. 659–675. doi:10.1016/S0045-7825(99)00432-6

[4] Fedkiw, R. P., "Coupling an Eulerian Fluid Calculation to a Lagrangian Solid Calculation with the Ghost Fluid Method," *Journal of Computational Physics*, Vol. 175, No. 1, 2002, pp. 200–224. doi:10.1006/jcph.2001.6935

[5] Arienti, M., Hung, P., Morano, E., and Shepherd, J. E., "A Level Set Approach to Eulerian-Lagrangian Coupling," *Journal of Computational Physics*, Vol. 185, No. 1, 2003, pp. 213–251. doi:10.1016/S0021-9991(02)00055-4

[6] Cirak, F., and Radovitzky, R., "A Lagrangian-Eulerian Shell-Fluid Coupling Algorithm Based on Level Sets," *Computers & Structures*, Vol. 83, Nos. 6–7, 2005, pp. 491–498. doi:10.1016/j.compstruc.2004.03.085

[7] Cottet, G., and Maitre, E., "A Level Set Method for Fluid-Structure Interactions with Immersed Surfaces," *Mathematical Models and Methods in Applied Sciences*, Vol. 16, No. 3, 2006, pp. 415–438. doi:10.1142/S0218202506001212

[8] Seo, J. H., and Mittal, R., "A Sharp-Interface Immersed Boundary Method with Improved Mass Conservation and Reduced Spurious Pressure Oscillations," *Journal of Computational Physics*, Vol. 230, No. 19, 2011, pp. 7347–7363. doi:10.1016/j.jcp.2011.06.003

[9] Lakshminarayan, V., Farhat, C., and Main, A., "An Embedded Boundary Framework for Compressible Turbulent Flow and Fluid-Structured and Unstructured Grids," *International Journal for Numerical Methods in Fluids*, Vol. 76, No. 6, 2014, pp. 366–395. doi:10.1002/fld.v76.6

[10] Chen, Z., Wu, Z., and Xiao, Y., "An Adaptive Immersed Finite Element Method with Arbitrary Lagrangian-Eulerian Scheme for Parabolic Equations in Time Variable Domains," *International Journal of Numerical Analysis and Modeling*, Vol. 12, No. 3, 2015, pp. 567–591.

[11] Gwak, M., Lee, Y., Kim, K., Cho, H., Shin, S. J., and Yoh, J. J., "All Eulerian Method of Computing Elastic Response of Explosively Pressurized Metal Tube," *Combustion Theory and Modelling*, Vol. 21, No. 2, 2017, pp. 293–308. doi:10.1080/13647830.2016.1223352

[12] Fadlum, E. A., Verzicco, R., Orlandi, P., and Mohd-Yusof, J., "Combined Immersed-Boundary Finite-Difference Methods for Three-Dimensional

Complex Flow Simulations," *Journal of Computational Physics*, Vol. 161, No. 1, 2000, pp. 35–60.
doi:10.1006/jcph.2000.6484

[13] Hu, X. Y., and Khoo, B. C., "An Interface Interaction Method for Compressible Multifluids," *Journal of Computational Physics*, Vol. 198, No. 1, 2004, pp. 35–64.
doi:10.1016/j.jcp.2003.12.018

[14] Gwak, M., Lee, Y., Kim, K., and Yoh, J. J., "Deformable Wall Effects on the Detonation of Combustible Gas Mixture in a Thin-Walled Tube," *International Journal of Hydrogen Energy*, Vol. 40, No. 7, 2015, pp. 3006–3014.
doi:10.1016/j.ijhydene.2014.12.127

[15] Kim, K., Gwak, M., and Yoh, J. J., "An Enhanced Particle Reseeding Algorithm for the Hybrid Particle Level Set Method in Compressible Flows," *Journal of Scientific Computing*, Vol. 65, No. 1, 2015, pp. 431–453.
doi:10.1007/s10915-014-9970-6

[16] Moorhead, S. B., "The Latest in Ship Weapon Launchers—The Vertical Launching System," *Naval Engineers Journal*, Vol. 93, No. 2, 1981, pp. 90–96.
doi:10.1111/nej.1981.93.issue-2

[17] Yagla, J. J., "Internal Ballistics of Weapon Launching Systems," *Naval Engineers Journal*, Vol. 95, No. 3, 1983, pp. 178–191.
doi:10.1111/nej.1983.95.issue-3

[18] Bertin, J. J., Berin, R. S., Yung, A., and Soohoo, G., "The Launch-Tube Flow-Field for a Vertical Launching System," *AIAA 26th Aerospace Sciences Meeting*, AIAA Paper 1988-0332, Jan. 1988.

[19] Lee, K. S., Hong, S. K., and Park, S. O., "Supersonic Jet Impingement Navier-Stokes Computations for Vertical Launching System Design Applications," *Journal of Spacecraft and Rockets*, Vol. 41, No. 5, 2004, pp. 877–886.
doi:10.2514/1.2594

[20] Saha, S., and Chakraborty, D., "Plume-Ducting System Design of Vertical Launcher Using Computational-Fluid-Dynamics Tools," *Journal of Spacecraft and Rockets*, Vol. 50, No. 3, 2013, pp. 715–718.
doi:10.2514/1.A32303

[21] Bhatti, M. A., *Fundamental Finite Element Analysis and Applications*, Wiley, Hoboken, NJ, 2006, pp. 340–499.

[22] Neto, E. A. S., Peric, D., and Owen, D. R. J., *Computational Methods for Plasticity*, Wiley, Hoboken, NJ, 2008, pp. 357–382.

[23] Moreno, J. P., "An Invitation to Plane Topology," *Australian Mathematical Society Gazette*, Vol. 29, No. 3, 2002, pp. 149–154.

[24] Kurganov, A., and Tadmor, E., "Solution of Two-Dimensional Riemann Problems for Gas Dynamics Without Riemann Problem Solvers," *Numerical Methods for Partial Differential Equations*, Vol. 18, No. 5, 2002, pp. 584–608.
doi:10.1002/(ISSN)1098-2426

[25] Cai, W., Thakre, P., and Yang, V., "A Model of AP/HTPB Composite Propellant Combustion in Rocket-Motor Environments," *Combustion Science and Technology*, Vol. 180, No. 12, 2008, pp. 2143–2169.
doi:10.1080/00102200802414915

[26] McBride, B. J., and Gordon, S., "Computer Program for Calculation of Complex Chemical Equilibrium Compositions and Applications," NASA RP-1311, 1996.

R. Schwane
Associate Editor